J. Fluid Mech. (2005), *vol.* 544, *pp.* 353–377.
doi:10.1017/S0022112005006725 Printed in the United Kingdom

Lubrication in a corner

By ROMAN STOCKER[1] AND A. E. HOSOI[2]

[1]Department of Civil and Environmental Engineering, Massachusetts Institute of Technology, 77 Massachusetts Avenue, Cambridge, MA 02139, USA
romans@mit.edu

[2]Department of Mechanical Engineering, Hatsopoulos Microfluids Laboratory, Massachusetts Institute of Technology, 77 Massachusetts Avenue, Cambridge, MA 02139, USA
peko@mit.edu

(Received 22 December 2003 and in revised form 7 December 2004)

A mathematical model for the evolution of a thin film in an interior corner region is presented. The model is based on the idea that the film can be considered thin everywhere in the η-direction if viewed in the new coordinate system $\xi = x^2 - y^2$, $\eta = 2xy$. Lubrication theory is applied to the governing equations written in this coordinate system. The exact integration of the mass conservation equation for a no-slip boundary condition yields a single evolution equation, which is integrated numerically. The evolution of a thin film driven by surface tension and gravity is predicted as a function of the Bond number and successfully compared to laboratory experiments.

1. Introduction

Studies on the behaviour of thin liquid films are of universal interest due to their extensive practical applications. Readily available reduced models can be used to investigate their evolution and stability in response to a wide range of physical forces. These films are important in industry, where they are used to coat and protect surfaces, such as automobile bodies, beverage containers and microelectronic components (Roy, Roberts & Simpson 2002), or as paints, adhesives and membranes. Biophysical applications include the liquid lining of the lungs (Grotberg 1994) where capillary–elastic instabilities can lead to collapse of a vessel (Rosenzweig & Jensen 2002), the film protecting the cornea of the eye (Wong, Fatt & Radke 1996) and the motion of contact lenses (Moriarty & Terrill 1996). In environmental processes, thin films appear in foam dynamics (Wasan, Koczo & Nikolov 1994), lava flows, gravity currents under water (Huppert 1982), and in the transport of bacteria in laminar flow over soil (Myers 2003). In agriculture, they play an important role in determining the effectiveness of agrochemicals such as insecticides and herbicides (Schwartz & Weidner 1995). Thin films may exhibit rich dynamics, including wave propagation, steepening, fingering and rupture (e.g. Bertozzi & Pugh 1998). The extensive literature on these topics is reviewed in Oron, Davis & Bankoff (1997) and Myers (1998).

Recently, considerable attention has been devoted to thin film flows over topography. In the coating of microelectronic components, for example, one aims to reduce the inside ('fat edges') and outside ('picture framing') corner defects (Schwartz & Weidner 1995). The shape of the interface is dictated by a competition between the substrate, which impresses its shape onto that of the interface – effectively contributing an additional capillary pressure – and surface tension, tending to flatten the free surface and to drive the solution to stable minimum-energy configurations

(Kalliadasis, Bielarz & Homsy 2000). Short-wavelength irregularities of the free surface are rapidly levelled by surface tension forces, while the long-term evolution is determined primarily by the topography of the substrate (Roy *et al.* 2002).

Unfortunately, a standard lubrication approach is *a priori* not expected to be accurate in the neighborhood of steep features, due to the small-slope assumption. Despite this limitation Stillwagon & Larson (1988, 1990) derived, and successfully compared to experiments, a single fourth-order, nonlinear, diffusion-like evolution equation describing the levelling of micron-sized isolated trenches by spin-coating under the influence of surface tension. Kalliadasis *et al.* (2000) extended this lubrication theory over topography to include an external body force, such as gravity, and found that the free surface develops a ridge just before the entrance to a trench, due to the capillary pressure gradient induced by the curvature of the substrate. Schwartz & Weidner (1995) took a different approach and adopted a locally orthogonal coordinate system that naturally fits an arbitrarily curved substrate where the film thickness is assumed to be small compared to the radius of curvature of the substrate. Roy *et al.* (2002) developed a more complex method, in which an artificial variable, proportional to the amount of liquid locally above the substrate, is used instead of the liquid thickness; gravity and inertia are included *a posteriori* via centre manifold techniques. The latter two studies both rely on the assumptions made by Stillwagon & Larson (1988) and no attempt is made at modelling sharp features such as a corner.

The evolution equation used by Stillwagon & Larson (1988, 1990) and Kalliadasis *et al.* (2000) assumes that the slopes of both the free surface and the substrate are small (Kalliadasis *et al.* 2000). The lubrication approximation is formally valid only for small-slope profiles and small capillary numbers (Mazouchi & Homsy 2001) and is expected to break down in the immediate vicinity of a sharp step (Kalliadasis *et al.* 2000). In such a geometry, one must apply the full Stokes equations. Mazouchi & Homsy (2001) investigated free-surface Stokes flow over topography with sharp edges using a boundary integral method, finding good agreement with lubrication theory for small capillary numbers even in the neighbourhood of steep features. This indicates that the area around the sharp step where lubrication breaks down is small and does not significantly affect the levelling of the trench, validating results by Stillwagon & Larson (1990) and Kalliadasis *et al.* (2000).

The application that originally motivated the present work is the 'fishbone' instability observed in filament stretching experiments (sketched in figure 1*c*) performed on polystyrene-based Boger fluids by Spiegelberg & McKinley (1996). This instability occurs exactly at the corner formed by two orthogonally intersecting thin films (figure 10*b* of Spiegelberg & McKinley 1996), a common configuration in extensional rheometers used in the study of complex fluids. For applications such as this in which the dominant physics occurs inside the corner region, as sketched in figure 1(*a*), the existing approaches described above are unsuitable because large gradients in the shape of the free surface develop and the slope cannot be small everywhere. Furthermore, the curvature of the substrate diverges at the corner. We propose a model that relies on a change of coordinates to address this gap in the thin-film literature. We then develop the lubrication approximation – based on this change of coordinates – for a film bounded by a solid corner. The analogous free-film geometry is addressed in Stocker & Hosoi (2004).

In contrast to the classical Landau–Levich problem (Landau & Levich 1942), where an infinite plate is pulled out from a deep pool of liquid, the film is thin along both walls in the configuration we are considering (figure 1*a*). Landau & Levich derived separate expressions for the thin film coating the plate and the meniscus in the deep

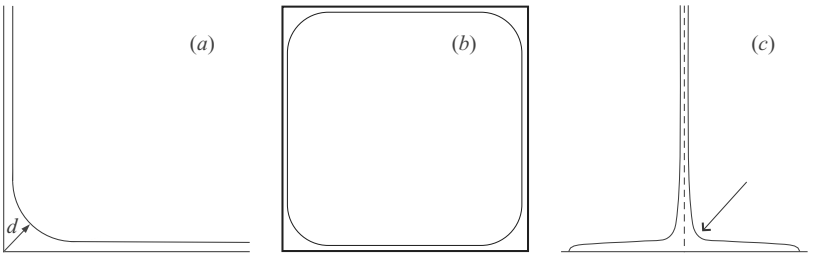

FIGURE 1. (*a*) Sketch of a thin film in an interior corner. d is the distance from the origin to the point on the free surface where $\xi = 0$ (i.e. $x = y$). (*b*) Cross-section of bubble flow in a square capillary, far from the bubble's ends. The thick line indicates the capillary, the thin line is the surface of the bubble, which is moving out of the page. Such non-axisymmetric bubbles form at small capillary numbers (<0.04). (*c*) Stretching of liquid filaments, as observed, for example, in rheological experiments. The arrow indicates the region where 'fishbone' instabilities were observed experimentally by Spiegelberg & McKinley (1996) in non-Newtonian fluids.

pool and closed the problem by matching curvatures. This approach differs from ours in two important respects. First, the deep pool is replaced by a thin film in which viscous stresses dominate. Second, the weakest link in the Landau–Levich solution – the matching – occurs precisely in the region of interest, the corner. The model proposed herein eliminates the need for a matching condition.

An example of a film evolving in a corner bounded by two solid walls is the flow of long gas bubbles in square or rectangular capillaries (Kolb & Cerro 1993*a*, *b*; Thulasidas, Abraham & Cerro 1995; Wong, Radke & Morris 1995; Bico & Queré 2002; Hazel & Heil 2002), sketched in figure 1(*b*). This mechanism has important applications in oil recovery from porous rocks, in the coating of tubes of square cross-section and in automotive or industrial monolithic reactors. For oil recovery, square capillaries provide a better model for the irregular and angular nature of the porous media and the thickness of the wetting film is a direct measure of the unrecoverable oil fraction (Kolb & Cerro 1993*b*). Theoretical analysis has been developed for axisymmetric bubbles (Kolb & Cerro 1993*a*, *b*; Thulasidas *et al.* 1995) valid when the capillary number is larger than 0.04 (Thulasidas *et al.* 1995). For smaller values, bubbles become non-axisymmetric and flatten out against the tube walls, creating liquid regions in the corners separated by thin flat films (figure 1*b*). In the reference frame of the bubble, the flow in these corner regions (sufficiently far away from both ends of the bubble) is an example of a thin film in a corner. Liquid corner regions also arise in the imbibition of a close-packed assembly of fibres (Bico & Queré 2002). Weislogel & Lichter (1998) and Weislogel (2001) investigated a similar geometry to ours, with capillary flow in a direction perpendicular to the plane of the corner.

After deriving the governing equations in the new coordinate system in the next section, lubrication theory is applied in § 3 to derive an evolution equation for a film with no-slip boundaries. Details of the derivations are presented in two Appendices. The numerical method applied in solving the evolution equation is detailed in § 4 and results are given in § 5. We chose not to perform a transverse linear stability analysis, since our focus in this paper is on presenting a method to develop lubrication theory in a corner and not on the physical mechanism responsible for instability in any particular context. Comparisons with experiments, designed to provide a test bed for the model, are presented in § 6. The final section discusses the limitations of the model and the modifications required for several applications.

2. Hyperbolic coordinates

2.1. *The governing equations in vector form*

The flow in an interior corner is considered, as sketched in figure 1(*a*). The momentum and continuity equations are, respectively,

$$-\frac{\nabla p}{\rho} + \nu\nabla^2 \boldsymbol{u} - g\hat{\boldsymbol{k}} = 0, \qquad \nabla \cdot \boldsymbol{u} = 0, \tag{2.1a, b}$$

where $\boldsymbol{u}$ is the velocity field, p is the pressure, ν is the kinematic viscosity, ρ is the density, g is the acceleration due to gravity and $\hat{\boldsymbol{k}}$ is the unit vertical vector, positive upwards. Here we consider low-Reynolds-number flows, thus inertial terms have been neglected in (2.1). We will consider two-dimensional systems, assuming no variation in the third dimension. The two stress boundary conditions at the free surface are

$$\hat{\boldsymbol{n}} \cdot \boldsymbol{\Pi} \cdot \hat{\boldsymbol{n}} = \sigma\kappa, \qquad \hat{\boldsymbol{t}} \cdot \boldsymbol{\Pi} \cdot \hat{\boldsymbol{n}} = 0, \tag{2.2a, b}$$

where $\hat{\boldsymbol{n}}$ and $\hat{\boldsymbol{t}}$ are the unit outward normal and tangent vectors to the free surface, respectively, σ is the surface tension, and $\kappa = -\nabla \cdot \hat{\boldsymbol{n}}$ is the curvature of the free surface. For a Newtonian fluid, the stress tensor is

$$\boldsymbol{\Pi} = \mu[\nabla \boldsymbol{u} + (\nabla \boldsymbol{u})^T] - p\boldsymbol{I}, \tag{2.3}$$

where $\mu = \rho\nu$ is the dynamic viscosity, $\boldsymbol{I}$ the identity matrix and ^{T} indicates a transpose matrix. Furthermore, conservation of mass and no-slip at the corner's walls will be imposed.

2.2. *The change of coordinates*

The fundamental idea presented herein is to exploit the fact that, at all positions along the wall, the film is thin if measured in a direction transverse to the wall. Cartesian coordinates (x, y) are not well suited for such an approximation, because the film is not everywhere thin in one of the two coordinate directions (or, equivalently, because the slope is not everywhere small). On the other hand, if we introduce the hyperbolic coordinate system

$$\xi = x^2 - y^2, \qquad \eta = 2xy, \tag{2.4a, b}$$

shown in figure 2, for all values of ξ (i.e. everywhere along the wall) the film can be treated as thin in the η-direction. Note that the Cartesian axes now correspond to $\eta = 0$, with η increasing with x and y in the first quadrant. The second coordinate, ξ, increases along the wall from large y towards large x, in the shape of hyperbolas. The change of coordinates (2.4) is a special case ($n = 2$) of the analytical conformal map transformation for a corner of angle π/n:

$$\xi = \mathrm{Re}[(x + \mathrm{i}y)^n], \qquad \eta = \mathrm{Im}[(x + \mathrm{i}y)^n], \tag{2.5a, b}$$

where Re and Im indicate the real and imaginary part, respectively. The derivations become cumbersome for arbitrary n. Here we will pursue the simplest and most interesting case of a square corner ($n = 2$).

The coordinate system (2.4) is orthogonal, since the mixed scale factor

$$\frac{\partial x}{\partial \xi}\frac{\partial x}{\partial \eta} + \frac{\partial y}{\partial \xi}\frac{\partial y}{\partial \eta} \tag{2.6}$$

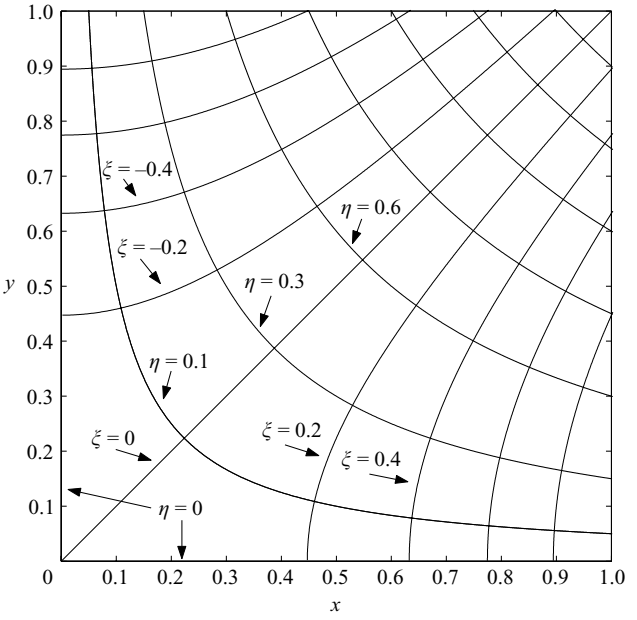

FIGURE 2. The hyperbolic coordinate system ($\xi = x^2 - y^2$, $\eta = 2xy$).

is everywhere zero. The scale factors associated with the ξ- and η-directions are equal and given by

$$s = \left[\left(\frac{\partial x}{\partial \xi} \right)^2 + \left(\frac{\partial y}{\partial \xi} \right)^2 \right]^{1/2} = \left[\left(\frac{\partial x}{\partial \eta} \right)^2 + \left(\frac{\partial y}{\partial \eta} \right)^2 \right]^{1/2} = \frac{1}{2\sqrt{r}}, \tag{2.7}$$

where $r = (\xi^2 + \eta^2)^{1/2} = x^2 + y^2$. The derivatives of (x, y) with respect to (ξ, η) – as well as the expressions for gradient, divergence and Laplacian in hyperbolic coordinates – are given in Appendix A.1. The coordinate transformation (2.4) is singular at the origin; however, this does not represent a problem since, excluding rupture at the origin, the free surface of the film never passes through the singularity.

2.3. *The governing equations in the hyperbolic coordinates*

Using (A 1), (A 2), (A 4), and (A 12), we can rewrite the governing equations (2.1) in hyperbolic coordinates:

$$\frac{\partial u}{\partial \xi} + \frac{\partial v}{\partial \eta} + f_1 u + f_2 v = 0, \tag{2.8a}$$

$$\frac{1}{\rho}\frac{\partial p}{\partial \xi} = \frac{\nu}{s}\left[\frac{\partial^2 u}{\partial \xi^2} + \frac{\partial^2 u}{\partial \eta^2} - \frac{1}{r^2}\left(\eta \frac{\partial v}{\partial \xi} - \xi \frac{\partial v}{\partial \eta} + \frac{u}{4} \right) \right] - g\frac{\partial y}{\partial \xi}, \tag{2.8b}$$

$$\frac{1}{\rho}\frac{\partial p}{\partial \eta} = \frac{\nu}{s}\left[\frac{\partial^2 v}{\partial \xi^2} + \frac{\partial^2 v}{\partial \eta^2} - \frac{1}{r^2}\left(-\eta \frac{\partial u}{\partial \xi} + \xi \frac{\partial u}{\partial \eta} + \frac{v}{4} \right) \right] - g\frac{\partial y}{\partial \eta}, \tag{2.8c}$$

where f_1, f_2, $\partial y/\partial \xi$ and $\partial y/\partial \eta$ are functions only of the position (ξ, η) and are defined in Appendix A.1. The explicit dependence of the equations on position represents an important variation with respect to Cartesian coordinates. The first two terms in the square brackets are the Laplacian of the scalar quantities u and v, while the remaining terms arise because the unit vectors $\hat{\boldsymbol{\xi}}$ and $\hat{\boldsymbol{\eta}}$ are position dependent (see Appendix A.2).

In order to transform the normal stress boundary condition (2.2a), the curvature κ in the new coordinates is computed from the unit outward normal vector (A 5) using (A 2b):

$$\kappa = -\nabla \cdot \hat{\boldsymbol{n}} = \frac{h''}{s(1+h'^2)^{3/2}} + \frac{h' f_1 - f_2}{s(1+h'^2)^{1/2}}, \tag{2.9}$$

where $\eta = h(\xi, t)$ is the position of the interface in hyperbolic coordinates and a prime denotes a derivative with respect to ξ. Using expression (A 7) for a Newtonian stress tensor together with (A 5), (A 6), and (2.9), allows us to write the stress boundary conditions (2.2) as

$$-p + \frac{2\mu}{s(1+h'^2)}\left[\frac{\partial v}{\partial \eta} - \frac{\xi u}{2r^2} + h'^2\left(\frac{\partial u}{\partial \xi} - \frac{\eta v}{2r^2}\right) + -h'\left(\frac{\partial v}{\partial \xi} + \frac{\partial u}{\partial \eta} + \frac{\eta u + \xi v}{2r^2}\right)\right] = \sigma\kappa, \tag{2.10a}$$

$$2h'\left(\frac{\partial v}{\partial \eta} - \frac{\partial u}{\partial \xi} + \frac{\eta v - \xi u}{2r^2}\right) + (1-h'^2)\left(\frac{\partial v}{\partial \xi} + \frac{\partial u}{\partial \eta} + \frac{\eta u + \xi v}{2r^2}\right) = 0. \tag{2.10b}$$

The last equation to be imposed is conservation of mass (or, equivalently, volume, since we assume a constant density), expressing the fact that the time rate of change of a volume element must equal the net volume flux from the neighbouring elements. In (ξ, η) the volume of liquid between ξ and $\xi + \Delta\xi$ is

$$\int_0^{h(\xi)} \int_{\xi}^{\xi+\Delta\xi} s^2 \,\mathrm{d}\xi \,\mathrm{d}\eta = \Delta\xi \int_0^{h(\xi)} s^2 \,\mathrm{d}\eta, \tag{2.11}$$

where we have used the fact that a volume element can be approximated as a rectangle of width $s\Delta\xi$ as $\Delta\xi \to 0$. The net flux into the element is

$$\int_0^{h(\xi)} u(\xi, \eta) s \,\mathrm{d}\eta - \int_0^{h(\xi+\Delta\xi)} u(\xi + \Delta\xi, \eta) s \,\mathrm{d}\eta. \tag{2.12}$$

As $\Delta\xi \to 0$, mass conservation therefore implies

$$\frac{\partial A}{\partial t} + \frac{\partial Q}{\partial \xi} = 0, \tag{2.13}$$

where

$$A = \int_0^{h(\xi)} s^2 \,\mathrm{d}\eta, \qquad Q = \int_0^{h(\xi)} u(\xi, \eta) s \,\mathrm{d}\eta. \tag{2.14a, b}$$

3. Lubrication theory

3.1. *The reduced equations*

In this section, lubrication theory is applied to the full governing equations (2.8), (2.10), and (2.13) to obtain a single evolution equation for the film 'thickness' $h(\xi, t)$. Such a reduced model relies on the existence of two widely disparate length scales. The advantages over an entirely numerical approach include avoiding the complexity of the original free-boundary problem, computational savings and a deeper understanding of the underlying physics. We begin by rescaling the governing equations (2.8), (2.10) and (2.13) by writing

$$\xi = L^2\tilde{\xi}, \qquad u = U\tilde{u}, \qquad t = T\tilde{t} = L\tilde{t}/U, \tag{3.1a–c}$$

$$\eta = L\,H\tilde{\eta}, \qquad v = V\tilde{v}, \qquad p = P\tilde{p}, \tag{3.1d–f}$$

where tildes denote dimensionless variables. Here L is the characteristic length scale along the layer, H is the characteristic thickness of the film, U and V are characteristic velocities along and across the layer, respectively, and P is the pressure scale. Since ($\xi = x^2 - y^2$, $\eta = 2xy$) are quadratic in the Cartesian coordinates, we have rescaled ξ by L^2 and η by $L\,H$. Therefore, $h(\xi, t)$ is not properly a thickness, but has dimensions of a length squared. In order to include the case of zero gravity, a characteristic velocity along the wall is defined in terms of viscosity and surface tension as $U = \sigma/\mu$. Thus, the characteristic time $T = L/U$ required for a fluid parcel with velocity U to travel across the length L of the layer, becomes $T = \mu L/\sigma$. Only dimensionless variables will be used from now on unless otherwise stated and the tildes will be dropped.

In the lubrication limit, it is natural to assume that the parameter $\epsilon = H/L$ is small and to expand the dependent variables u, v and p in powers of ϵ:

$$u = u_0 + \epsilon^2 u_2 + O(\epsilon^4), \tag{3.2a}$$

$$v = v_0 + \epsilon^2 v_2 + O(\epsilon^4), \tag{3.2b}$$

$$p = p_0 + \epsilon^2 p_2 + O(\epsilon^4). \tag{3.2c}$$

The expansion parameter ϵ is proportional to the filling fraction, the detailed relation depending on the initial condition. Quantities depending on the position (ξ, η) are also made dimensionless (f_1 scales like L^2, f_2 like ϵ/L^2, and s like $1/L$). We rescale (2.8), (2.10), and (2.13), substitute for (3.2), and retain only the lowest-order terms in ϵ. The position-dependent terms f_1, f_2, and s also involve the expansion parameter ϵ and could in principle be expanded in powers of ϵ. However, this makes the equations singular at $\xi = 0$. Further details on this point are given in § 3.3, where we discuss an approximate solution, derived by retaining only the leading-order terms for the position-dependent quantities.

The continuity equation (2.8*a*) yields a relation between the two velocity scales, $V = \epsilon U$. The Bond number $Bo = \rho g L^2/\sigma$ represents the relative importance of gravity and surface tension. The momentum equation along ξ (2.8*b*) suggests a pressure scale $P = \sigma/(\epsilon^2 L)$, which is standard for lubrication theory (Myers 2003), and thus reduces to

$$\frac{\partial p_0}{\partial \xi} = 2\left(\xi^2 + \epsilon^2\eta^2\right)^{1/4} \frac{\partial^2 u_0}{\partial \eta^2} - \epsilon^2 Bo \frac{\partial y}{\partial \xi}, \tag{3.3}$$

where $\partial y/\partial \xi$ is a function of position only, given in (A 1*c*). The momentum equation along η (2.8*c*) becomes

$$\frac{\partial p_0}{\partial \eta} = -\epsilon^2 Bo \frac{\partial y}{\partial \eta}, \tag{3.4}$$

while the stress boundary conditions at the free surface $\eta = h$ are

$$-p_0 = \epsilon^3 \kappa, \qquad \frac{\partial u_0}{\partial \eta} = 0. \tag{3.5a, b}$$

In (3.3), (3.4) and (3.5) we chose to retain gravity and surface tension to leading order, since we are interested in the case in which both effects enter into the dominant force balance. In particular, we have retained the full curvature in (3.5*a*), as done first by Ruschak (1978). This ensures that the potential energy is the same as that of the full equations, so that 'exact surfaces of static equilibrium are also equilibrium solutions of the model' (Eggers & Dupont 1994), these being the states that minimize potential energy.

3.2. *The evolution equation*

The system of equations at $O(1)$, namely (2.13), (3.3), (3.4), and (3.5), can now be solved subject to the no-slip boundary condition. Integrating (3.4) in η, from η to h, and imposing the normal stress boundary condition (3.5a) at $\eta = h$, yields an expression for pressure:

$$p_0 = -\epsilon^3 \kappa + \epsilon^2 Bo\,[y|_h - y|_\eta], \tag{3.6}$$

where y is given in terms of ξ and η in (A 1a) and the vertical bar indicates at which value of η a quantity is evaluated. Substituting (3.6) into (3.3) and rearranging, we find

$$\frac{\partial^2 u_0}{\partial \eta^2} = \frac{\epsilon^2 \gamma(\xi)}{2(\xi^2 + \epsilon^2 \eta^2)^{1/4}}, \tag{3.7}$$

where

$$\gamma(\xi) = -\epsilon \kappa' + Bo \left.\frac{\partial y}{\partial \xi}\right|_h. \tag{3.8}$$

The curvature gradient κ' is obtained after some algebra as

$$\kappa' = \frac{2\alpha}{\beta^3} h''' - \frac{6\epsilon^2 \alpha}{\beta^5} h'(h'')^2 - \frac{3(h - \xi h')(\xi + \epsilon^2 h h')}{2\alpha^7 \beta}, \tag{3.9}$$

where $\alpha = (\xi^2 + \epsilon^2 h^2)^{1/4}$, $\beta = (1 + \epsilon^2 h'^2)^{1/2}$, and

$$\left.\frac{\partial y}{\partial \xi}\right|_h = \frac{1}{2\sqrt{2}(\sqrt{\xi^2 + \epsilon^2 h^2} - \xi)^{1/2}} \left[\frac{\xi + \epsilon^2 h h'}{\sqrt{\xi^2 + \epsilon^2 h^2}} - 1\right]. \tag{3.10}$$

Again, we will not approximate (3.10) to avoid incurring singularities at $\xi = 0$.

The integration of (3.7) can be carried out exactly in terms of the hypergeometric functions ${}_2F_1$ (Abramowitz & Stegun 1965). Making use of (3.5b) and the no-slip condition $u_0 = 0$ at $\eta = 0$, we eventually find

$$u_0(\eta, \xi) = \frac{\gamma(\xi)|\xi|^{3/2}}{3} \left[1 - {}_2F_1\left(-\frac{1}{2}, -\frac{3}{4}; \frac{1}{2}; -\frac{\epsilon^2 \eta^2}{\xi^2}\right) - \frac{3\epsilon^2 \eta h}{2\xi^2} {}_2F_1\left(\frac{1}{4}, \frac{1}{2}; \frac{3}{2}; -\frac{\epsilon^2 h^2}{\xi^2}\right)\right]. \tag{3.11}$$

Note that the first hypergeometric function is evaluated at η, while the second one is evaluated at h. When we substitute (3.11) into the mass conservation equation (2.13), all integrals except for one can be evaluated exactly. In particular:

$$\frac{\partial}{\partial t} \int_0^{h(\xi)} s^2 \,\mathrm{d}\eta = \frac{\partial}{\partial t} \int_0^{h(\xi)} \frac{1}{4(\xi^2 + \epsilon^2 \eta^2)^{1/2}} \,\mathrm{d}\eta = \frac{1}{4(\xi^2 + \epsilon^2 h^2)^{1/2}} \frac{\partial h}{\partial t}. \tag{3.12}$$

In addition, the following two indefinite integrals are used:

$$\int \frac{1}{(\xi^2 + \epsilon^2 \eta^2)^{1/4}} \,\mathrm{d}\eta = \frac{h}{|\xi|^{1/2}} \, {}_2F_1\left(\frac{1}{4}, \frac{1}{2}; \frac{3}{2}; -\frac{\epsilon^2 \eta^2}{\xi^2}\right), \tag{3.13a}$$

$$\int \frac{\eta}{(\xi^2 + \epsilon^2 \eta^2)^{1/4}} \,\mathrm{d}\eta = \frac{2}{3\epsilon^2} (\xi^2 + \epsilon^2 \eta^2)^{3/4}. \tag{3.13b}$$

Combining these results, we find the evolution equation

$$\frac{1}{4(\xi^2 + \epsilon^2 h^2)^{1/2}} \frac{\partial h}{\partial t} - \frac{\epsilon}{6} \frac{\partial}{\partial \xi} \left\{h^2 \gamma(\xi) R\left(\frac{\xi}{\epsilon h}\right)\right\} = 0, \tag{3.14}$$

where

$$R(z)=|z|\left\{\left[-2+\left(1+\frac{1}{z^2}\right)^{3/4}\right]{}_2F_1\left(\frac{1}{4},\frac{1}{2};\frac{3}{2};-\frac{1}{z^2}\right)+\int_0^1 \frac{{}_2F_1\left(-\frac{1}{2},-\frac{3}{4};\frac{1}{2};-\frac{\hat{\eta}^2}{z^2}\right)}{(1+\hat{\eta}^2/z^2)^{1/4}}\,\mathrm{d}\hat{\eta}\right\}. \tag{3.15}$$

We were unable to evaluate the last integral analytically.

In unidirectional lubrication theories that use arclength along the substrate as the long coordinate (Schwartz & Weidner 1995; Roy *et al.* 2002), the second derivative of the substrate's curvature (which is already a delta function) enters the evolution equation. This represents a strong singularity and cannot be handled numerically without approximations. By adopting our change of coordinates, the only remnant of the substrate's sharp corner is a weak singularity in (3.14) arising from the absolute value in (3.15). Assuming that the gradient of the free-surface curvature κ' ($\approx h'''$) can offset the discontinuity, it can be shown that h is at least C^2, that is the singularity shows up only in the third and higher derivatives. This weak discontinuity is easily overcome by the numerical solution, as demonstrated in the following sections by the smoothness of all our numerical profiles.

3.3. *An approximation of the evolution equation*

The price to pay for avoiding the strong singularity due to the sharp corner, is that we must retain ϵ in the final evolution equation (or, alternatively, in the initial condition). In most formulations, though not all (e.g. Hosoi & Mahadevan 1999), this does not occur. The reason for retaining ϵ in the position-dependent terms is that lubrication theory is based on the relative magnitude of variations in the dependent variables, that is derivatives. No assumptions are made about quantities that depend on position alone. This is not an issue in Cartesian coordinates, as purely position-dependent terms never arise. While one may not call our approach 'standard lubrication theory' due to this perhaps spurious retention of the expansion parameter ϵ, it is nevertheless clear that our formulation provides a straightforward way of dealing with a geometry that is out of reach for most other methods, without resorting to the full Stokes equations. For this reason, the filling fraction remains as a parameter, through ϵ.

In this paper, all integrals in the mass conservation equation but one could be solved exactly. On the other hand, it is to be expected that in more complex scenarios – such as a domain stretching in time or a non-Newtonian stress tensor – one would not be able to perform the integration analytically. The expansion of the position-dependent terms would then possibly allow an exact integration. It is therefore important to have an understanding of the accuracy of this approximation. In this section we derive an approximate evolution equation obtained by expanding the position-dependent terms in ϵ. In the present case the only such term is $1/s$ in (2.8*b*), which reduces to

$$\frac{1}{s}=2(\xi^2+\epsilon^2\eta^2)^{1/4}\approx 2|\xi|^{1/2}\left[1+O\left(\frac{\epsilon\eta}{\xi}\right)^2\right]. \tag{3.16}$$

The difference introduced by the approximation in (3.16) in the governing equations is that $|\xi|^{1/2}$ replaces $(\xi^2+\epsilon^2\eta^2)^{1/4}$ in (3.3), yielding

$$\frac{\partial^2 u_0}{\partial\eta^2}=\frac{\epsilon^2\gamma(\xi)}{2|\xi|^{1/2}} \tag{3.17}$$

instead of (3.7). The right-hand side of (3.17) is now independent of η, allowing two straightforward integrations in η. Use of the boundary conditions at $\eta=0$ and h

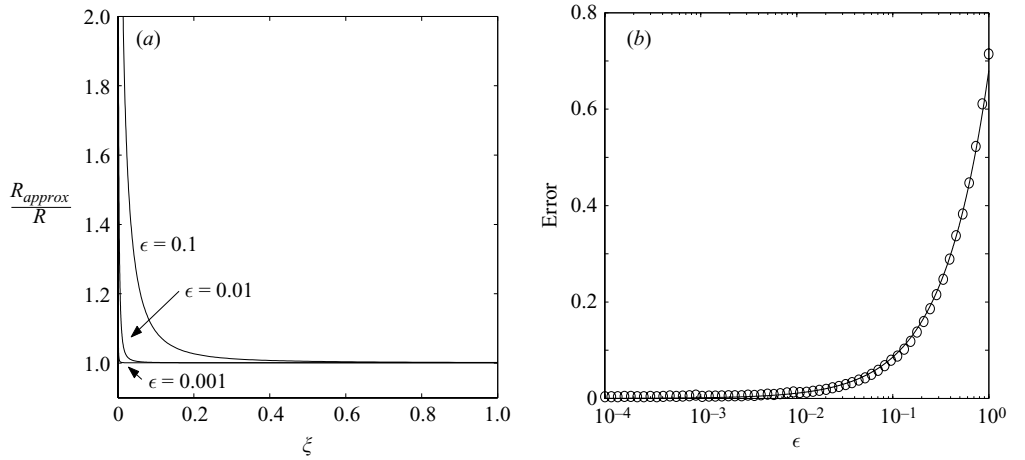

FIGURE 3. (*a*) Ratio of R_{approx} (3.20) to R (3.15) as a function of the along-wall coordinate ξ, for $h = 1$ and three values of ϵ, using $N = 5000$ grid points. $R_{approx}/R \to 1$ as $\xi \to \infty$, indicating that R_{approx} is a good approximation to R unless ξ is very close to zero. (*b*) The error incurred by approximating R with R_{approx}, computed as the integral of $R_{approx}/R - 1$ over $10^{-5} < \xi \leqslant 1$, shown as circles. The error grows approximately like $\epsilon^{0.9}$ (the solid line represents $0.67\epsilon^{0.9}$) and vanishes as $\epsilon \to 0$.

yields

$$u_0 = \frac{\epsilon^2 \gamma(\xi)}{2|\xi|^{1/2}} \left(\frac{\eta^2}{2} - \eta h \right). \tag{3.18}$$

Note that this velocity profile is parabolic as expected, but it is parabolic in the new coordinate system. When this expression is substituted into the mass conservation equation (2.13), the following integrals arise:

$$\frac{1}{2} \int_0^{h(\xi)} \eta^2 s \, \mathrm{d}\eta = \frac{h}{10\epsilon^2} \left[(\xi^2 + \epsilon^2 h^2)^{3/4} - |\xi|^{3/2} \, {}_2F_1 \left(\frac{1}{2}, \frac{1}{4}; \frac{3}{2}; -\frac{\epsilon^2 h^2}{\xi^2} \right) \right], \tag{3.19a}$$

$$\int_0^{h(\xi)} \eta h s \, \mathrm{d}\eta = \frac{h}{2} \int_0^{h(\xi)} \frac{\eta}{(\xi^2 + \epsilon^2 \eta^2)^{1/4}} \, \mathrm{d}\eta = \frac{h}{3\epsilon^2} \left[(\xi^2 + \epsilon^2 h^2)^{3/4} - |\xi|^{3/2} \right]. \tag{3.19b}$$

We eventually find the approximate evolution equation to be of the same form as (3.14), with $R(z)$ in (3.15) replaced by

$$R_{approx}(z) = |z| \left[-1 + \frac{7}{10} \left(1 + \frac{1}{z^2} \right)^{3/4} + \frac{3}{10} {}_2F_1 \left(\frac{1}{4}, \frac{1}{2}; \frac{3}{2}; -\frac{1}{z^2} \right) \right], \tag{3.20}$$

where $z = \xi/(\epsilon h)$.

In order to use this approximation confidently, we need to quantify the error we are introducing. It is evident that $R_{approx} \to R$ when $|z| \gg 1$ (i.e. $|\xi| \gg \epsilon h$). However, as $z \to 0$, $R \to 1$ while R_{approx} diverges, indicating that in general R_{approx} is not a good representation of R close to $\xi = 0$. This is shown in figure 3(*a*), where the ratio R_{approx}/R is plotted for $h = 1$ and three values of ϵ. In computing R, the integral in (3.15) was evaluated numerically using the trapezoidal rule. The ratio R_{approx}/R always diverges as $\xi \to 0$, but it asymptotes to 1 as $\xi \to \infty$ in all three cases, showing that R_{approx} accurately approximates R for all values of ξ, except for the region closest to $\xi = 0$. The discrepancy is barely discernible in figure 3(*a*) for $\epsilon = 0.001$, but grows with ϵ. On the other hand, we can show that the influence of this region is small.

Figure 3(*b*) shows that the error incurred by approximating R by R_{approx} tends to zero as $\epsilon \to 0$. That error was computed as the integral of $R_{approx}/R - 1$ over $0 < \xi \leqslant 1$. Since $R_{approx} \to \infty$ as $|\xi| \to 0$, we started the numerical integration at $\xi = 10^{-5}$ and verified that the changes induced by a smaller starting value are negligible. The error grows approximately like $\epsilon^{0.9}$. Thus, the integral contribution of the point-wise singularity to the overall evolution of the film is subdominant (mathematically, a portion of the integrand diverges, but its contribution to the integral is nevertheless small) and we can expect accurate results for thin films even when the position-dependent terms are approximated. This solution is effectively equivalent to solving left and right of $\xi = 0$ and then arguing that – as the approximation breaks down only in a tiny neighbourhood of $\xi = 0$ – any errors that may be introduced are bounded owing to exact mass conservation.

As the approximation (3.20) involves no significant loss in accuracy, but considerable saving in computational time (since we avoid the numerical evaluation of the integral in (3.15)), all simulations in this paper are based on the approximate solution. The fact that the outcomes agree well with both theoretical and experimental results – as will be seen – further justifies the use of the approximate solution. In particular, in no case was a singular behaviour near $\xi = 0$ observed. In the next section we describe the numerical scheme we used to solve (3.14) with $R(z)$ replaced by $R_{approx}(z)$.

4. Numerical solution of the evolution equation

In our numerical solution the fourth-order equation (3.14) is first split into two second-order equations, by defining an auxiliary variable $f = h''$ (which is not the curvature, since we are not in Cartesian coordinates). Denoting the term in curly brackets in (3.14) as q, the numerical scheme becomes

$$F_i^{n+1} = \frac{1}{\left[\xi_i^2 + \epsilon^2 \left(h_i^{n+1}\right)^2\right]^{1/2}} \frac{h_i^{n+1} - h_i^n}{\Delta t} - \frac{\epsilon}{6} \frac{\left(q_{i+1/2}^{n+1} - q_{i-1/2}^{n+1}\right)}{(\Delta_i^+ - \Delta_i^-)/2} = 0, \tag{4.1a}$$

$$G_i^{n+1} = f_i^{n+1} - m_i^+ h_{i+1}^{n+1} - m_i h_i^{n+1} - m_i^- h_{i-1}^{n+1} = 0, \tag{4.1b}$$

where the subscript i represents the ith grid point, and the free surface is located at (ξ_i, h_i^{n+1}) at time step $n+1$. The integration was performed on a non-uniform grid, so that a higher grid-point density could be adopted closest to the corner. Details of the grid are given in Appendix B. The distance between grid point i and its two neighbours $i \pm 1$ is $\Delta_i^{\pm} = |\xi_{i\pm1} - \xi_i|$. First derivatives were approximated by centred differences. Second derivatives were computed on a three-point stencil as a weighted average of the first forward and backward derivatives, as in (4.1*b*), with $m_i^+ = 2/[\Delta_i^+(\Delta_i^+ + \Delta_i^-)]$, $m_i = -2/(\Delta_i^+ \Delta_i^-)$ and $m_i^- = 2/[\Delta_i^-(\Delta_i^+ + \Delta_i^-)]$. Equation (4.1*a*) was discretized in flux-conserving form in order to ensure numerical mass conservation. At each grid point i only the outward flux, $q_{i+1/2}$, was computed, while for the inward flux, $q_{i-1/2}$, we reused the outward flux of its left neighbour $i-1$.

The scheme is backward in time and uses an adaptive time step based on a step-doubling algorithm (Press *et al.* 1992) to minimize the computational time. At each step, two solutions are computed: the first (S_B) by using the full time step Δt, the second (S_S) by taking two steps of length $\Delta t/2$. If the error $|S_B - S_S|$, averaged over all grid points, is larger than a specified tolerance (typically 10^{-4}), the step is rejected and repeated after halving the time step. Otherwise, the step is accepted and an extrapolated value $S = 2S_B - S_S$ of the solution is computed which achieves $O(\Delta t^2)$

accuracy. The next time step is then increased by a factor inversely proportional to the error.

The solution at any step was found by solving (4.1) implicitly. The Jacobian of the functions F and G in (4.1) was computed analytically, resulting in a heptadiagonal matrix (three non-zero diagonals on each side of the main diagonal) that was inverted using standard Gaussian elimination for banded matrices. A Newton iteration procedure correctly showed quadratic convergence and after a maximum of four Newton iterations the residual never exceeded 10^{-14}.

As the four boundary conditions for the fourth-order differential equation (3.14) we chose no-flux and zero (Cartesian) slope at both ends ($\xi = \pm 1$). These conditions must be expressed in the hyperbolic system. For slopes, we have

$$\frac{\mathrm{d}y_s}{\mathrm{d}x} = \frac{h(\epsilon^2 h h' + \xi - r)}{2r(r-\xi)} \approx \epsilon\left(h' - \frac{h}{2\xi}\right), \tag{4.2a}$$

$$\frac{\mathrm{d}x_s}{\mathrm{d}y} = -\frac{\epsilon h}{2r} - \frac{\epsilon^3 h^2 h'}{2r(r+\xi)} \approx -\epsilon\left(h' - \frac{h}{2\xi}\right), \tag{4.2b}$$

where (4.2a) is used if the free surface is written as $y_s(x)$ (numerically more accurate for $y > x$, i.e. at $\xi = -1$), while (4.2b) is used if the free surface is written as $x_s(y)$ (for $\xi = 1$). Since $\epsilon h \ll |\xi|$ is always true at the boundaries, we can use the Taylor-approximated relations in (4.2). A similar reasoning applies for the flux boundary condition. The flux in (x, y) is the volume of fluid crossing a line $x =$ constant (for $x > y$) or $y =$ constant (for $y > x$) in unit time. The flux in (ξ, η), on the other hand, is the volume of fluid crossing a line $\xi =$ constant in unit time. While it is cumbersome to transform a flow rate given in (x, y) into its (ξ, η)-equivalent, we note that in the lubrication limit the two flow rate definitions coincide to within a term of $O(\epsilon^2)$ when $\epsilon h \ll |\xi|$. This is certainly the case at the boundaries, since far away from the corner the lines of constant ξ tend to coincide with the lines of constant x (for $x > y$) or constant y (for $y > x$). Thus, the flux specified in the (x, y) system can be directly applied in the (ξ, η) system. Further details of the numerical scheme, along with results from convergence tests, are given in Appendix B.

5. Results

We begin by testing the ability of the model to capture the evolution of a thin film under surface tension alone ($Bo = 0$). Figure 4(a) shows the case of an initially L-shaped profile for $\epsilon = 0.04$. For this initial condition, the expansion parameter, ϵ, can be related to the filling fraction, F_R, of the unit Cartesian box by $F_R = \epsilon(1 - \ln\epsilon)$. The two can thus be used interchangeably as a measure of the film thickness. For $\epsilon = 0.04$, $F_R = 0.169$. Surface tension progressively reduces the gradient of curvature everywhere and eventually the fluid assumes the shape of a quarter of a circle (profile at $t = 10^5$), whose radius of curvature is determined only by F_R. As expected, different initial conditions (e.g. a hyperbola) with the same filling fraction led to the same steady state. In particular, the model correctly captures the fact that – irrespective of the particular initial condition – the sharp corner in the substrate never causes any singularity in the free surface of the film.

The steady state for several values of F_R is shown in figure 5(a). For $F_R < F_{Rcr} = 1 - \pi/4 \simeq 0.215$, the liquid retracts towards the corner, where it forms a quarter of a circle. For $F_R > F_{Rcr}$, there is enough fluid for the curvature to be the same everywhere. In all cases, the curvature gradient is everywhere zero (except in the small transition

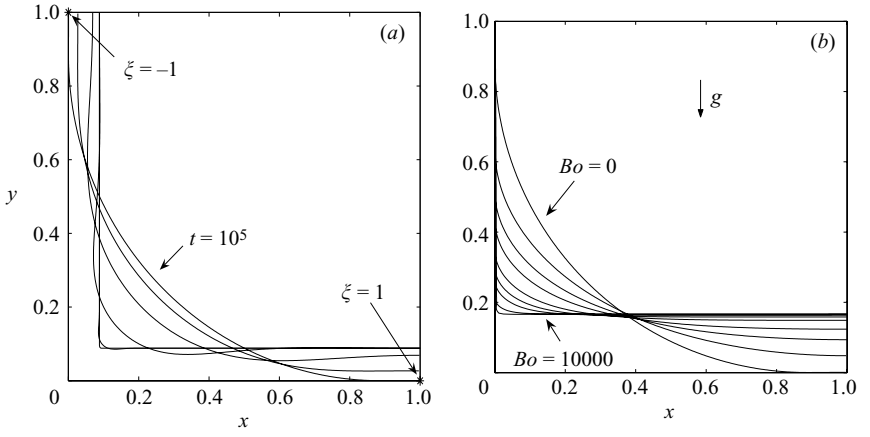

FIGURE 4. (*a*) Snapshots of the evolution of a thin film governed by surface tension ($Bo = 0$) for $F_R = 0.169$ ($\epsilon = 0.04$). The profiles correspond to the dimensionless times $t = 0, 3.6 \times 10^{-4}$, 0.67, 22.9, 112.6, 10^5. By $t = 10^5$ the profile has reached steady state. (*b*) The steady state of a draining thin film governed by gravity and surface tension for several values of Bo (0, 4, 10, 20, 50, 100, 200, 1000, 10000) and $F_R = 0.169$ ($\epsilon = 0.04$). Gravity forces the film to drain from the vertical wall and to form a pool at the bottom, whose size increases with Bo. In both panels the initial condition consists of an L-shaped region of liquid with a sharp corner. No-flux and zero-slope boundary conditions were imposed at both ends ($\xi = \pm 1$).

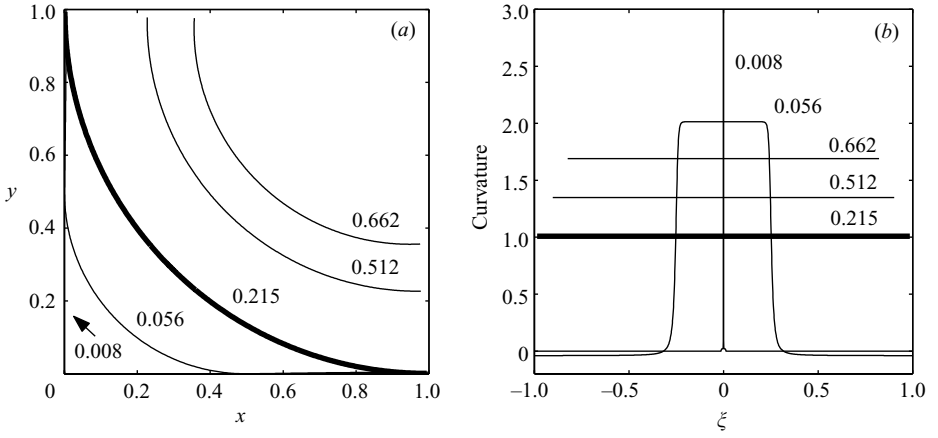

FIGURE 5. Steady-state profile (*a*) and curvature (*b*) of a thin film governed by surface tension ($Bo = 0$) for several values of F_R, indicated in the plots. For the critical filling fraction $F_R = 1 - \pi/4 \simeq 0.215$ ($\epsilon = 0.055$) the steady-state configuration is a quarter of a circle with curvature 1 (thicker lines in (*a*) and (*b*)). All cases were simulated up to $t = 10^5$ and no further evolution occurred for larger times. The constant value of the curvature indicates that the steady-state profiles predicted by the model are correct, as they correspond to the states of minimum energy. Note that in (*a*) the curve for $F_R = 0.008$ is indistinguishable from the axes at this resolution. The initial and boundary conditions are as in figure 4.

region between the two regions of constant curvature) and the curvature of the circular region (figure 5*b*) matches the one computed theoretically, since the steady state is the state that minimizes the surface area (here, the perimeter), for a given F_R. Note that the model performs accurately even for rather large values of ϵ, the largest filling fraction in figure 5 corresponding to $\epsilon = 0.3$.

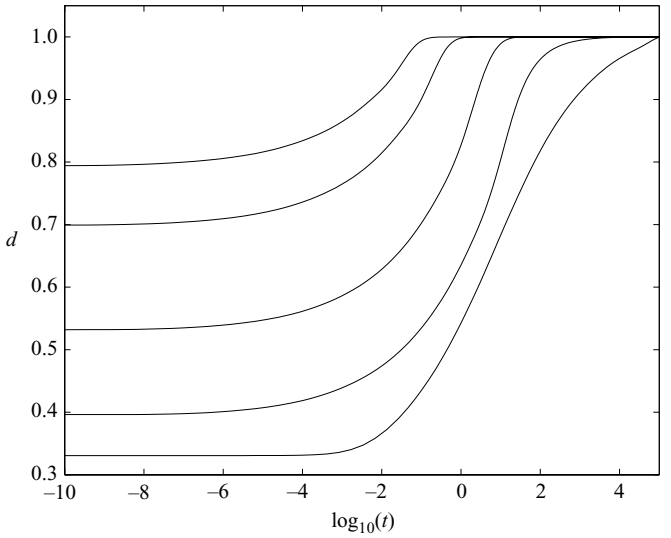

FIGURE 6. The time scale for evolution to steady state for $Bo = 0$ and $F_R = 0.008, 0.215, 0.330, 0.512, 0.662$ (bottom to top). Thinner films take longer to reach steady state due to the larger influence of viscous drag. d is the distance indicated in figure 1 (a), normalized by its steady-state value. The initial and boundary conditions are as in figure 4.

The time scale required to reach steady state as a function of the filling fraction can be inferred from figure 6. Here, the distance from the origin of the free-surface point lying on $x = y$ (that is, $\xi = 0$) – normalized by its steady-state value – is plotted versus time. Evolution is faster for larger filling fractions. The film reaches steady state after approximately $t = 0.1$ for $F_R = 0.662$ and takes 10^6 times longer for $F_R = 0.008$. Thus, for small filling fractions the evolution is very slow. This reflects the fact that the viscous drag exerted by the boundaries plays a more important role when the film is thin.

The typical velocity profile across a thin film in lubrication theory over a solid unidirectional substrate is parabolic (e.g. Myers 2003). In § 3.3 we showed that – if the position-dependent terms in the governing equations are also expanded in ϵ – the resulting velocity profile (3.18) is parabolic in η, which corresponds to a quartic in Cartesian coordinates. This quartic dependence is strongest near the corner and reduces to the expected Cartesian parabolic profile in the far field. On the other hand, the full velocity profile (3.11) is not exactly parabolic in η, and we expect the difference to be more pronounced nearest to the corner. Figure 7 compares the shape of u_0 from (3.11) to the approximate form (3.18), each normalized by its maximum value, as we are only interested in the shape of the profile. The normalized profiles depend on ϵ and ξ only through the ratio $\epsilon/|\xi|$. Figure 7(a) compares the two velocity profiles for $\epsilon/|\xi| = 10^5$, while figure 7(b) shows the maximum deviation of u_0 from a parabola as a function of $\epsilon/|\xi|$. For each value of $\epsilon/|\xi|$, the deviation at each η was computed as the relative difference between the two normalized velocities defined in figure 7 (a). Away from the corner (large $|\xi|$) and for very thin films (small ϵ), the velocity profile is indistinguishable from parabolic. However, even very close to the corner (small $|\xi|$) and for relatively thick films (large ϵ), the relative deviation of u_0 from parabolic never exceeds 3.5%. For example, for $\epsilon = 0.01$, the velocity profile is everywhere parabolic to within 1%, except for the region $|\xi| < 0.01$ closest to the corner.

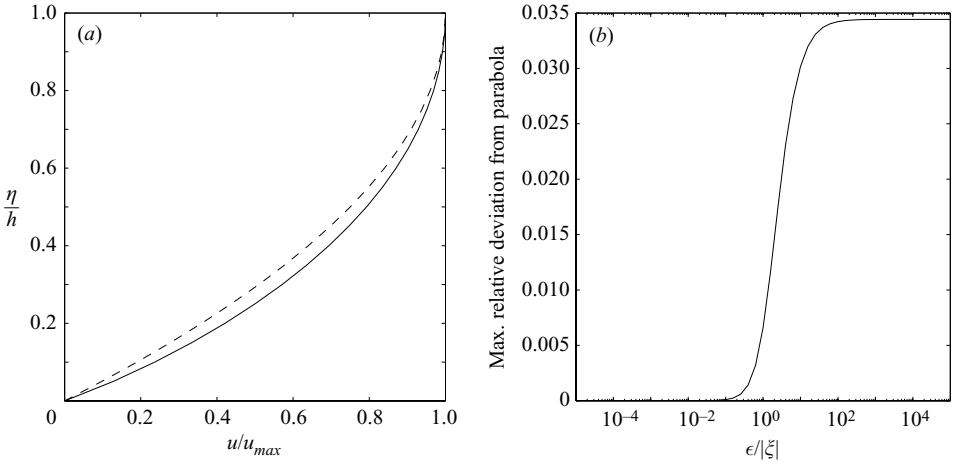

FIGURE 7. (*a*) The full velocity profile ((3.11), solid line) and the approximate velocity profile ((3.18), dashed line) for $\epsilon/|\xi| = 10^5$ and $h = 1$. The approximate velocity is exactly parabolic in η. Each velocity has been normalized by its value at $\eta = h$. (*b*) The maximum relative deviation of the full velocity profile (3.11) from a parabolic one (in η/h) as a function of $\epsilon/|\xi|$.

We should emphasize again that the parabolic dependence is in the hyperbolic – not the Cartesian – coordinates.

When $Bo \neq 0$, the evolution is governed by the competition between gravity and surface tension. Gravity destroys the symmetry about $\xi = 0$: the film drains down from the vertical wall and forms a pool along the bottom. This behaviour is accentuated for larger Bo. Figure 4(*b*) shows the steady-state shapes for several values of Bo. The fact that some fluid is retained on the vertical wall by surface tension even at steady state is due to the symmetry boundary condition applied at $\xi = -1$. As Bo increases, more fluid drains from the vertical wall and the pool at the bottom becomes larger. It is straightforward to show that for this steady case, (3.14) correctly reduces to the Young–Laplace equation for a static meniscus (see e.g. Landau & Lifschitz 1987).

We verified that the model can also capture, at least qualitatively, the initial stages of the evolution of a liquid film coating a ceiling near a vertical wall. In this case, gravity drives the fluid away from the ceiling, either by drainage along the vertical wall or by dripping. Lateral drainage prevails when F_R is large and Bo is small. For small F_R and large Bo, the film becomes unstable and forms steady-state pendant drops before it has the time to drain down the wall, as shown in figure 8. We observed up to five drops, the number of drops increasing with Bo. Yiantsios & Higgins (1989) investigated the formation of drops in a thin viscous film, showing that, for small Bo, steady-state pendant drops are possible and correctly predicted by lubrication theory. Using their notation, all the steady-state cases in figure 8 qualify as small-Bo cases. Furthermore, their theory predicts the drop's length to decrease with Bo, a trend that is successfully captured by our model. Larger Bo cannot be achieved as the numerical film ruptures. This is also in line with Yiantsios & Higgins' conclusion that lubrication theory fails at large Bo, when the interface becomes highly convoluted. The decay in amplitude of the drops towards the corner is due to the asymmetry introduced by the presence of the vertical wall. We did not concern ourselves extensively with pendant drops, since our change of coordinates is certainly not the simplest approach to this geometry. However, the fact that our model is able to capture steady-state pendant drops correctly gives further confidence in its validity.

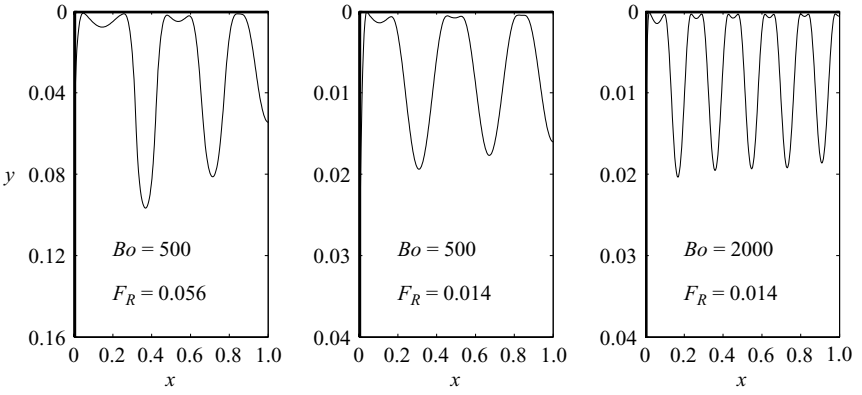

FIGURE 8. Formation of steady-state pendant drops. $F_R = 0.056$ and 0.014 correspond to $\epsilon = 0.01$ and 0.002, respectively. The solid wall is indicated by a thick line. Only a portion of the vertical axis is shown. The initial and boundary conditions are as in figure 4.

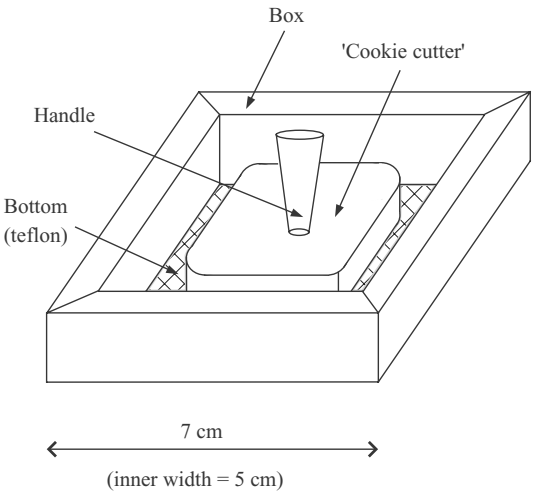

FIGURE 9. Schematic of the experimental device (not to scale). The square box is made out of Plexiglas and a solution of water and glycerol is injected in the gap – shown as a hatched region – between the box and the 'cookie-cutter'. The experiment consists of lifting the 'cookie-cutter' and observing how the fluid evolves under surface tension. In a second set of experiments the box is tilted to investigate the effect of gravity. No 'cookie-cutter' is used in this case.

6. Comparison with experiments

As a further validation of the model, a comparison with a set of simple experiments was carried out. The experiments concern the evolution of a thin layer of fluid under the combined action of surface tension and gravity. The experimental device, shown in figure 9, consists of a square Plexiglas box without a lid, with a Teflon coated bottom to maximize the contact angle with the fluid and to minimize pinning of the contact line. The inner size of the box is $5 \times 5\,\mathrm{cm}^2$. A smaller, 'cookie-cutter'-like shape, $4.4 \times 4.4\,\mathrm{cm}^2$, was positioned inside the box, so that the two were concentric and their four sides parallel, forming a 0.3 cm wide gap between the inner sides of the box and the shape. The corners of the shape were smooth, with a radius of curvature

of 0.3 cm. The gap was filled with a glycerol-water solution, dyed with thymol blue for visualization purposes, whose typical depth was less than 1 mm. The 'cookie-cutter' was removed suddenly by pulling it up vertically.

Digital pictures of the steady state were taken and image processing was used to reconstruct the position of the interface. After converting the image to a grey-scale colour map, the interface was defined by setting a threshold value of grey. The reconstructed interface is insensitive to small changes in this threshold value. Only experiments in which symmetry among the four corners was preserved were retained, to obtain an easy comparison of the steady state with that obtained from the model, in which a zero-slope and zero-flux boundary conditions at both ends were imposed. F_R for the model was determined by integrating the area of the reconstructed profile. One example of the comparison is shown in figure 10 for $Bo = 0$ and $F_R = 0.19$.

One discrepancy between the model and the experiments derives from the fact that the experiment did not evolve to the theoretical steady state (e.g. figure 5). In particular, the thickness of the film at $\xi = \pm 1$ did not tend to zero. This discrepancy is due to three-dimensional effects. Since the profile has a finite depth and a non-trivial shape in the third dimension, an additional curvature exists. The latter is opposite in sign to the main curvature and becomes important as the film approaches steady state. Ultimately, when the depth of the film becomes comparable to its width, the evolution is arrested. In addition, pinning effects cannot completely be avoided, despite the fact that a very hydrophobic substance (Teflon) was chosen to coat the bottom of the box. This contributes to the premature arrest of the evolution. Note that viscosity is irrelevant in determining the steady-state shape – determined only by F_R and Bo – but influences the time scale of the evolution. To obtain a comparison with the experiments, the numerical model was integrated up to steady state and the profile at some time t that most closely matched the experimental observation was chosen. The best match was determined by minimizing the absolute value of the difference of h from the model and from the experiments. We are thus assuming that the evolution in the experiments follows the predictions up to a certain time, then stops due to three-dimensional effects. This points both to the limitation and the accuracy of the model. The limitation is clear in that any three-dimensional effects cannot be captured in the current analysis. On the other hand, the comparison in figure 10 shows that the model works extremely well, in that it almost perfectly captures the shape of the steady-state profile, up to the point where three-dimensional effects become dominant and arrest the evolution.

Figure 11(a, b) reinforces this conclusion, showing that the agreement is good irrespective of the filling fraction. Unfortunately, no consistent pattern was observed in the times of best fit, nor could they be reliably linked to the adjustment process in the experiment. The experiments could be enhanced by eliminating the pinning effects, which would result in a better comparison with the predicted steady state. However, these limitations are due to the experimental setup and since the focus of this paper is on the model, we did not proceed further in the experimental investigation.

The effects of gravity were introduced by slightly tilting the experimental device. In this case, no 'cookie-cutter' was used. Instead, a quantity of fluid was injected along the four walls of the box, so as to wet all of them. Most of the fluid was injected adjacent to one of the four sidewalls while the box was held with its bottom horizontal. Viscosity prevented the fluid from flowing under this configuration. The box was then tilted suddenly by a small angle (2.3°) so that the fluid started to flow down towards the opposite wall evolving under gravity and surface tension, and eventually reached steady state. The image processing and the method of comparison with the model

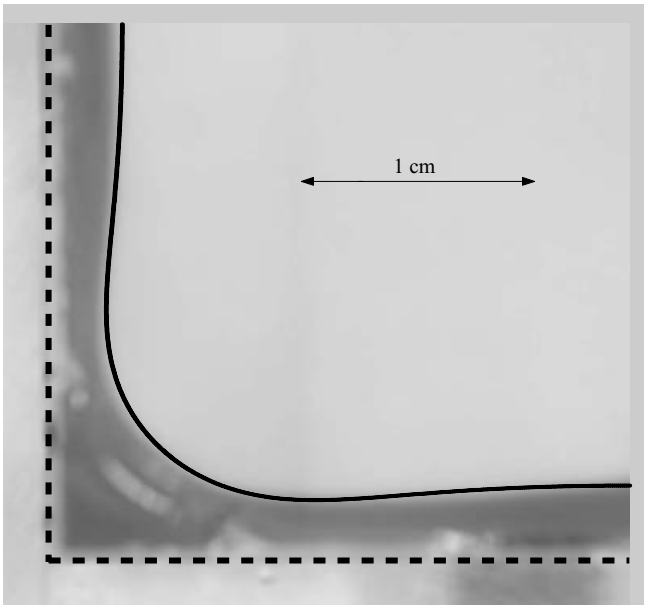

FIGURE 10. The steady state of a thin film governed by surface tension ($Bo = 0$): model prediction (thick line) versus experimental result (background picture). The filling fraction is $F_R = 0.19$ ($\epsilon = 0.047$). The dashed line indicates the position of the walls of the box. Note that the steady state is different from the one in figure 4(a) due to three-dimensional effects. The initial and boundary conditions for the simulation are as in figure 4.

were the same as in the previous case. Figure 11(c, d) shows results for $Bo = 15$ and two values of F_R.

While the experiments demonstrated that the model correctly reproduces the evolution of a thin film in a corner under surface tension and gravity, they also pointed out the importance of three-dimensional effects. The applicability of our two-dimensional model therefore needs to be carefully assessed on a case-by-case basis.

7. Discussion

We have derived an evolution equation for the flow of a thin film in a corner region and applied it to simple test cases. While the focus of this paper has been the development of a new method to apply lubrication theory in a corner, it is hoped that this approach will be helpful in many practical situations where thin films have to negotiate a corner. It is now appropriate to discuss the flow configuration in more detail, as well as the advantages and the limitations of this method, in conjunction with its possible applications.

Moffatt (1964) described the asymptotic flow of a viscous fluid near a corner of arbitrary angle θ. He found that an infinite geometric progression of eddies can develop, whose size and intensity fall off rapidly due to viscosity. When the sides of the corner are two solid walls, as in the case treated here, eddies can form for $\theta < 146°$. In our configuration, Moffatt's semi-infinite fluid domain is replaced by a thin layer having a free surface, prompting the question of whether eddies can still arise. While our lowest-order model is intrinsically unable to capture eddies (as the lowest-order velocity is approximately parabolic in the new coordinates), it is most accurate in the limit of extremely thin films, where eddies are least likely to develop. Thus, if

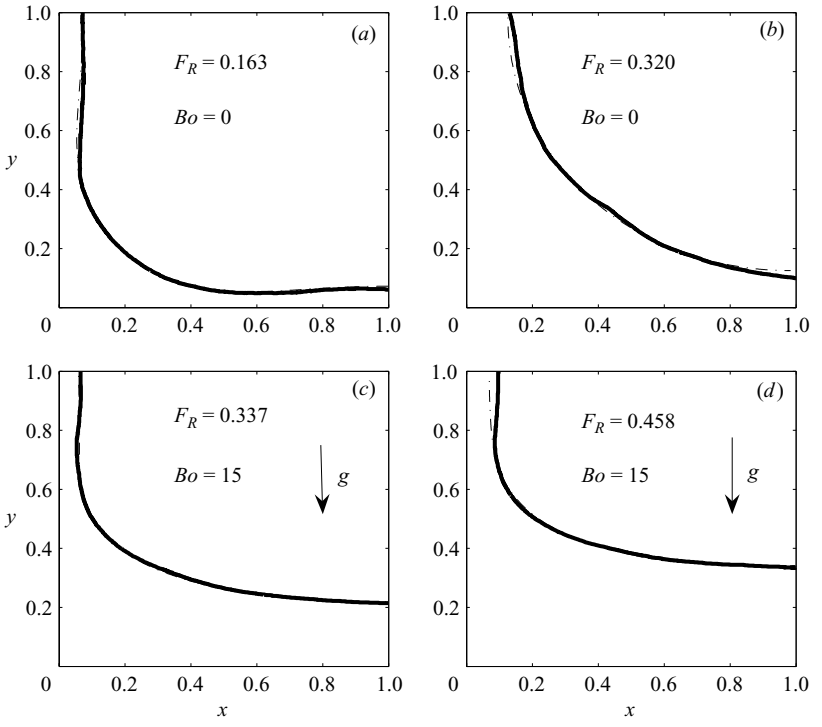

FIGURE 11. The steady state of a thin film governed by surface tension for different values of F_R and Bo: model predictions (dash-dotted line) versus experimental results (thick solid line). The two lines are on top of each other almost everywhere, indicating the good agreement between theory and experiments. The interface for the experiments was reconstructed digitally as explained in the text. The initial and boundary conditions for the simulations are as in figure 4.

Moffatt eddies are to form – a question best answered by solving the full Stokes flow equations – we would expect them in thicker films, where our approximation loses validity. It is interesting to note that eddies cannot form in a square corner when at least one of the two sides is not a solid wall (Moffatt 1964).

The advantage of our approach over a full numerical solution of the original governing equations is apparent in terms of the computational time – each of the simulations presented in this paper took only a few seconds on a 1.8 GHz Pentium 4. Furthermore, aside from the complexities of any numerical code dealing with a free surface, this geometry presents additional difficulties in defining a two-dimensional grid since, as the film becomes thinner, the cells become more and more elongated, eventually making a fully numerical scheme unstable. A clever choice of the grid in a finite element method would be one derived from our change of coordinates (see figure 2). Of course, this choice is not feasible when using finite differences, unless the equations are solved in the (ξ, η) coordinate system. Compared to more general lubrication approaches developed for thin films over topography (e.g. Roy *et al.* 2002), ours has the advantage of being simple both in the formulation and in the implementation. In addition, our method is specifically tailored to a sharp corner, where the substrate's curvature and its gradient become singular. In our approach, this singularity does not prevent exact integration of the mass conservation equation.

It is interesting to compare the present approach with the method of spines, originally developed by Kistler & Scriven (1983) (see also Heil & White 2002). In that

method, the film thickness is measured in the direction of certain pre-determined vectors – the spines – originating from the substrate. Conditions are imposed on the choice of the spines such that they do not intersect inside the fluid domain. Conceptually, this has some similarity with our approach, as we measure the thickness of the film along η. Lines of constant ξ could then be interpreted as curved spines, while the orthogonality of the coordinate system guarantees that our 'spines' do not intersect. With respect to ours, the method of spines has the advantage of being applicable to more general substrates. On the other hand, Heil & White (2002) showed that for highly curved substrates lubrication theory implemented using the method of spines does not ensure conservation of volume. They therefore developed a modified lubrication equation by introducing an appropriately chosen film density. However, they recognize that this *ad hoc* modification is not 'rational' in the sense of a long-wavelength asymptotic theory. In this respect, our change of coordinates has the merit of implicitly ensuring volume conservation, as well as being a more direct application of the traditional lubrication approach, based solely on the recognition that the film is everywhere thin if measured along η. Recently Jensen, Chini & King (2004) applied the method of spines to a lubrication model of an interior corner, again using a modified film density to ensure volume conservation.

The application of our model to the 'fishbone' instability of Spiegelberg & McKinley (1996), which originally motivated the present study, would require three main modifications. First, a non-Newtonian stress tensor would make the analytical integration of mass conservation more difficult. In general, we expect additional evolution equations associated with the fluid's constitutive relation (Schultz 1987; Olagunju 1999). Second, the asymmetric stretching of the domain must be taken into account (e.g. only along y, not along x). Third, 'mixed' boundary conditions must be used – no-slip on the bottom plate and symmetry across the centreline of the vertical filament. A linear stability analysis could then be performed numerically to (perhaps) capture the 'fishbone' instability. We did not perform a stability analysis on our solution as Spiegelberg & McKinley's experiments exhibit no instability when Newtonian fluids are used.

8. Conclusions

We have shown that lubrication theory can be used in an interior corner following an appropriate change of coordinates. The equations of motion were written in a hyperbolic coordinate system and the assumption that the liquid film is everywhere thin led to a single evolution equation for its thickness. The full curvature and gravity terms were retained. The simple η-dependence of the lowest-order velocity field allowed us to integrate the full equation of mass conservation exactly (to within one integral), with the great advantage of ensuring conservation of mass. We showed that care must be taken when ξ becomes small, due to the presence of position-dependent terms that, if approximated, make the equations singular at $\xi = 0$. However, even when such an approximation is made, the effects on the profile evolution and steady state are negligible for small film thicknesses. The numerical integration of the evolution equation has been described and implemented. The outcomes were successfully compared to theoretical results and simple laboratory experiments on a thin film in a corner evolving under surface tension and gravity.

We would like to thank Darren Crowdy, David Vener, Constantin Pozrikidis and José Bico for many useful discussions during the early stage of this manuscript. This research was partially supported by 3M and by NSF grant 0243591.

Appendix A. Details of the hyperbolic coordinates

This Appendix provides more details on the derivations in § 2 and § 3.

A.1. *Change of coordinates*

The following (dimensional) expressions were used in the change of coordinates $\xi = x^2 - y^2$, $\eta = 2xy$ (all notation is defined in the text):

$$y = \left(\frac{r-\xi}{2}\right)^{1/2}, \qquad x = \left(\frac{r+\xi}{2}\right)^{1/2}, \tag{A 1a, b}$$

$$\frac{\partial x}{\partial \eta} = -\frac{\partial y}{\partial \xi} = \frac{y}{2r}, \qquad \frac{\partial x}{\partial \xi} = \frac{\partial y}{\partial \eta} = \frac{x}{2r}, \tag{A 1c, d}$$

$$\frac{\partial r}{\partial \xi} = \frac{\xi}{r}, \qquad \frac{\partial r}{\partial \eta} = \frac{\eta}{r}, \tag{A 1e, f}$$

$$\frac{\partial s}{\partial \xi} = -\frac{\xi}{4r^{5/2}}, \qquad \frac{\partial s}{\partial \eta} = -\frac{\eta}{4r^{5/2}}, \tag{A 1g, h}$$

$$f_1 = \frac{1}{s}\frac{\partial s}{\partial \xi} = -\frac{\xi}{2r^2}, \qquad f_2 = \frac{1}{s}\frac{\partial s}{\partial \eta} = -\frac{\eta}{2r^2}. \tag{A 1i, j}$$

The expressions for gradient, divergence, and Laplacian in the hyperbolic coordinates, for example applied to the pressure field p and the velocity field $\boldsymbol{u} = u\hat{\boldsymbol{\xi}} + v\hat{\boldsymbol{\eta}}$ are (e.g. Arfken 1970)

$$\nabla p = \frac{1}{s}\frac{\partial p}{\partial \xi}\hat{\boldsymbol{\xi}} + \frac{1}{s}\frac{\partial p}{\partial \eta}\hat{\boldsymbol{\eta}}, \tag{A 2a}$$

$$\nabla \cdot \boldsymbol{u} = \frac{1}{s^2}\left[\frac{\partial (us)}{\partial \xi} + \frac{\partial (vs)}{\partial \eta}\right], \tag{A 2b}$$

$$\nabla^2 \boldsymbol{u} = \nabla \cdot \nabla \boldsymbol{u} = \frac{1}{s^2}\left[\frac{\partial}{\partial \xi}\left(\frac{\partial \boldsymbol{u}}{\partial \xi}\right) + \frac{\partial}{\partial \eta}\left(\frac{\partial \boldsymbol{u}}{\partial \eta}\right)\right], \tag{A 2c}$$

where $\hat{\boldsymbol{\xi}}$ and $\hat{\boldsymbol{\eta}}$ are the unit vectors along the hyperbolic coordinate axes, given by

$$\hat{\boldsymbol{\xi}} = \frac{\left((r+\xi)^{1/2}, -(r-\xi)^{1/2}\right)}{\sqrt{2r}} = \left(\frac{x}{\sqrt{r}}, -\frac{y}{\sqrt{r}}\right), \tag{A 3a}$$

$$\hat{\boldsymbol{\eta}} = \frac{\left((r-\xi)^{1/2}, (r+\xi)^{1/2}\right)}{\sqrt{2r}} = \left(\frac{y}{\sqrt{r}}, \frac{x}{\sqrt{r}}\right). \tag{A 3b}$$

The full expression for the Laplacian is derived in § A.2. The unit vector $\hat{\boldsymbol{k}}$ appearing in the gravity term in (2.1a) transforms as

$$\hat{\boldsymbol{k}} = \frac{1}{s}\frac{\partial y}{\partial \xi}\hat{\boldsymbol{\xi}} + \frac{1}{s}\frac{\partial y}{\partial \eta}\hat{\boldsymbol{\eta}}. \tag{A 4}$$

The position of the free surface in hyperbolic coordinates is described by $\mathscr{F}(\xi, \eta) = \eta - h(\xi) = 0$. The outward unit vector $\hat{\boldsymbol{n}}$ normal to the free surface can thus be computed using (A 2a) as

$$\hat{\boldsymbol{n}} = \frac{\nabla \mathscr{F}}{|\nabla \mathscr{F}|} = \frac{1}{|\nabla \mathscr{F}|}\left(\frac{1}{s}\frac{\partial \mathscr{F}}{\partial \xi}\hat{\boldsymbol{\xi}} + \frac{1}{s}\frac{\partial \mathscr{F}}{\partial \eta}\hat{\boldsymbol{\eta}}\right) = \frac{-h'\hat{\boldsymbol{\xi}} + \hat{\boldsymbol{\eta}}}{(1+h'^2)^{1/2}}, \tag{A 5}$$

while the unit tangent vector is

$$\hat{\boldsymbol{t}} = \frac{\hat{\boldsymbol{\xi}} + h'\hat{\boldsymbol{\eta}}}{(1+h'^2)^{1/2}}. \tag{A 6}$$

Using (A 2a) again, the stress tensor $\boldsymbol{\Pi}$ in (2.3) becomes:

$$\boldsymbol{\Pi} = \begin{pmatrix} -p + \dfrac{2\mu}{s}\left(\dfrac{\partial u}{\partial \xi} - \dfrac{\eta v}{2r^2}\right) & \dfrac{\mu}{s}\left(\dfrac{\partial v}{\partial \xi} + \dfrac{\partial u}{\partial \eta} + \dfrac{\eta u + \xi v}{2r^2}\right) \\ \dfrac{\mu}{s}\left(\dfrac{\partial v}{\partial \xi} + \dfrac{\partial u}{\partial \eta} + \dfrac{\eta u + \xi v}{2r^2}\right) & -p + \dfrac{2\mu}{s}\left(\dfrac{\partial v}{\partial \eta} - \dfrac{\xi u}{2r^2}\right) \end{pmatrix}. \tag{A 7}$$

A.2. *Laplacian*

The Laplacian of $\boldsymbol{u} = u\hat{\boldsymbol{\xi}} + v\hat{\boldsymbol{\eta}}$ appearing in the viscous terms of the momentum equations is somewhat lengthy to compute because the unit vectors $\hat{\boldsymbol{\xi}}$ and $\hat{\boldsymbol{\eta}}$ (A 3) are position-dependent, resulting in

$$\begin{aligned} \nabla^2 \boldsymbol{u} = \frac{1}{s^2}\Bigg[& \frac{\partial^2 u}{\partial \xi^2}\hat{\boldsymbol{\xi}} + \frac{\partial^2 v}{\partial \xi^2}\hat{\boldsymbol{\eta}} + 2\frac{\partial u}{\partial \xi}\frac{\partial \hat{\boldsymbol{\xi}}}{\partial \xi} + 2\frac{\partial v}{\partial \xi}\frac{\partial \hat{\boldsymbol{\eta}}}{\partial \xi} + u\frac{\partial^2 \hat{\boldsymbol{\xi}}}{\partial \xi^2} + v\frac{\partial^2 \hat{\boldsymbol{\eta}}}{\partial \xi^2} \\ & + \frac{\partial^2 u}{\partial \eta^2}\hat{\boldsymbol{\xi}} + \frac{\partial^2 v}{\partial \eta^2}\hat{\boldsymbol{\eta}} + 2\frac{\partial u}{\partial \eta}\frac{\partial \hat{\boldsymbol{\xi}}}{\partial \eta} + 2\frac{\partial v}{\partial \eta}\frac{\partial \hat{\boldsymbol{\eta}}}{\partial \eta} + u\frac{\partial^2 \hat{\boldsymbol{\xi}}}{\partial \eta^2} + v\frac{\partial^2 \hat{\boldsymbol{\eta}}}{\partial \eta^2}\Bigg]. \end{aligned} \tag{A 8}$$

The first derivatives of the unit vectors are

$$\frac{\partial \hat{\boldsymbol{\xi}}}{\partial \xi} = \frac{\eta}{2r^2}\hat{\boldsymbol{\eta}}, \qquad \frac{\partial \hat{\boldsymbol{\eta}}}{\partial \xi} = -\frac{\eta}{2r^2}\hat{\boldsymbol{\xi}}, \qquad \frac{\partial \hat{\boldsymbol{\xi}}}{\partial \eta} = -\frac{\xi}{2r^2}\hat{\boldsymbol{\eta}}, \qquad \frac{\partial \hat{\boldsymbol{\eta}}}{\partial \eta} = \frac{\xi}{2r^2}\hat{\boldsymbol{\xi}}. \tag{A 9a–d}$$

Since the second derivatives do not naturally split up into a $\hat{\boldsymbol{\xi}}$ and an $\hat{\boldsymbol{\eta}}$ component, dot products with $\hat{\boldsymbol{\xi}}$ and $\hat{\boldsymbol{\eta}}$ must be taken. This yields

$$\frac{\partial^2 \hat{\boldsymbol{\xi}}}{\partial \xi^2} = -\frac{\eta^2}{4r^4}\hat{\boldsymbol{\xi}} - \frac{\eta\xi}{r^4}\hat{\boldsymbol{\eta}}, \qquad \frac{\partial^2 \hat{\boldsymbol{\eta}}}{\partial \xi^2} = -\frac{\eta^2}{4r^4}\hat{\boldsymbol{\eta}} + \frac{\eta\xi}{r^4}\hat{\boldsymbol{\xi}}, \tag{A 10a, b}$$

$$\frac{\partial^2 \hat{\boldsymbol{\xi}}}{\partial \eta^2} = -\frac{\xi^2}{4r^4}\hat{\boldsymbol{\xi}} + \frac{\eta\xi}{r^4}\hat{\boldsymbol{\eta}}, \qquad \frac{\partial^2 \hat{\boldsymbol{\eta}}}{\partial \eta^2} = -\frac{\xi^2}{4r^4}\hat{\boldsymbol{\eta}} - \frac{\eta\xi}{r^4}\hat{\boldsymbol{\xi}}, \tag{A 10c, d}$$

where we have used

$$\frac{\partial}{\partial \xi}\left(\frac{1}{r^{1/2}}\right) = -\frac{\xi}{2r^{5/2}}, \qquad \frac{\partial}{\partial \eta}\left(\frac{1}{r^{1/2}}\right) = -\frac{\eta}{2r^{5/2}}, \tag{A 11a, b}$$

$$\frac{\partial}{\partial \xi}\left(\frac{1}{r^{5/2}}\right) = -\frac{5\xi}{2r^{9/2}}, \qquad \frac{\partial}{\partial \eta}\left(\frac{1}{r^{5/2}}\right) = -\frac{5\eta}{2r^{9/2}}. \tag{A 11c, d}$$

We can now rewrite (A 8) by separating the terms contributing to the ξ-momentum equation ($(\nabla^2 \boldsymbol{u})\cdot\hat{\boldsymbol{\xi}}$) from those contributing to the η-momentum equation ($(\nabla^2 \boldsymbol{u})\cdot\hat{\boldsymbol{\eta}}$). After some simplifications we find:

$$(\nabla^2 \boldsymbol{u})\cdot\hat{\boldsymbol{\xi}} = \frac{1}{s^2}\left[\frac{\partial^2 u}{\partial \xi^2} + \frac{\partial^2 u}{\partial \eta^2} - \frac{1}{r^2}\left(\eta\frac{\partial v}{\partial \xi} - \xi\frac{\partial v}{\partial \eta} + \frac{u}{4}\right)\right], \tag{A 12a}$$

$$(\nabla^2 \boldsymbol{u})\cdot\hat{\boldsymbol{\eta}} = \frac{1}{s^2}\left[\frac{\partial^2 v}{\partial \xi^2} + \frac{\partial^2 v}{\partial \eta^2} - \frac{1}{r^2}\left(-\eta\frac{\partial u}{\partial \xi} + \xi\frac{\partial u}{\partial \eta} + \frac{v}{4}\right)\right]. \tag{A 12b}$$

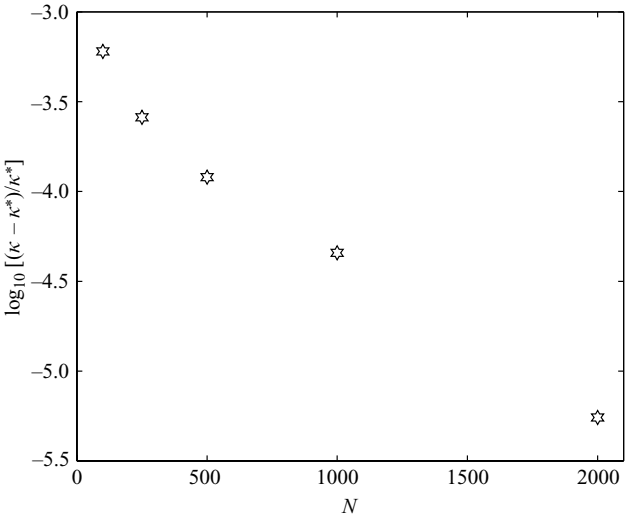

FIGURE 12. Relative error in the predicted steady-state curvature versus the number of grid points N for $Bo = 0$ and $F_R = 0.215$ ($\epsilon = 0.055$). κ is the curvature predicted from the model, κ^* is the theoretical curvature associated with the minimum surface configuration. The curvature from the model is computed as the average over $-0.5 \leqslant \xi \leqslant 0.5$.

Appendix B. Details of the numerical solution

This Appendix provides details on the numerical scheme used to integrate the evolution equation (3.14). The grid along ξ is determined as follows. Once the filling fraction F_R and the number of grid points N have been chosen, the first $N/2$ grid points are taken to be $(x_i, y_i) = (\Delta, 1-(i-1)\,\mathrm{d}y)$, for $i = 1 \ldots N/2$, with $\Delta = 1 - \sqrt{1 - F_R}$ and $\mathrm{d}y = (1 - \Delta - 2/N)/(N/2 - 1)$. The remaining $N/2$ grid points are found by symmetry about $x = y$. The ξ_i coordinate of the ith grid point is then $\xi_i = x_i^2 - y_i^2$. For this grid, $-\xi_{max} < \xi < \xi_{max}$, where $\xi_{max} = 1 - \Delta^2$. The grid points are therefore uniformly spaced along the Cartesian axes, so the density of grid points is parabolically increasing with ξ as $\xi \to 0$. This method avoids $\xi = 0$ being a grid point, a necessary precaution here since the approximate version of the evolution equation is used (see § 3.3 for more details). The initial condition $h_i = 2x_i y_i$ then corresponds to a film of uniform thickness Δ along both Cartesian axes (an L-shape).

Numerical tests were carried out for $F_R = F_{Rcr} = 0.215$, $Bo = 0$ and $N = 500$. The initial and boundary conditions were the same as in figure 4. The total integration time was $t = 10^5$, enough in all cases to achieve steady state. The effect of varying the number of grid points N can be seen from figure 12, where the error in the steady-state curvature is plotted against N. The steady-state curvature is constant over ξ and equal to one, since $F_R = F_{Rcr}$. However, a small correction is required due to the change of coordinates. At $t = 0$, $-\xi_{max} < \xi < \xi_{max}$ corresponds to the unit Cartesian box. As the film evolves, it becomes thinner at $\xi = \pm\xi_{max}$, thus corresponding to a box slightly smaller than the unit box in Cartesian coordinates. This artificial shrinking of the domain implies that the amount of fluid F_R needs to be accommodated in a smaller-than-unity box. Thus, the expected curvature is slightly larger than the theoretical one, its exact value being dependent on N. While this is admittedly an artifact of the numerical scheme and is described further below, its effect is of $O(\epsilon)$. (One could apply the boundary conditions at a ξ-position that is variable in time, according to the thickness of the film at the boundary, making the grid time-dependent. This

would introduce an additional complication that was not pursued in this paper.) In particular, it can be seen that the curvature predicted by the model converges towards the expected one as the number of grid points increases. $N = 500$ was considered sufficient for the purposes of this paper.

The fluid volume A (i.e. the area) can be computed as:

$$A = \int_{\xi} \int_{0}^{\epsilon h(\xi)} s^2 \, \mathrm{d}\eta \, \mathrm{d}\xi = \frac{1}{4} \int_{\xi} \ln \left[\frac{\epsilon h + \sqrt{\xi^2 + \epsilon^2 h^2}}{|\xi|} \right] \mathrm{d}\xi. \tag{B 1}$$

The loss of volume over $t = 10^5$ was always less than 0.4%, which can be attributed to the large values attained by R_{approx} (3.20) for small $|\xi|$.

The numerical scheme was implemented in Fortran. Fortran's built-in hypergeometric function routine is too inaccurate for our purposes. Thus we approximated the hypergeometric functions piece-wise using polynomials. The logarithm ($\log_{10}$) of the hypergeometric function's argument was split into 100 intervals, from -6 to $+4$ in increments of 0.1. In each interval, an nth-order polynomial was fitted to the logarithm of the hypergeometric function, with the best-fit coefficients determined using Matlab. We found that $n = 14$ resulted in the best compromise between accuracy and stability. Ultimately, this is equivalent to using a table of numbers for the hypergeometric functions, but has the advantage of obtaining a high accuracy – better than 10^{-10} for all values of the argument of the hypergeometric functions – without storing an excessive amount of data.

REFERENCES

Abramowitz, M. & Stegun, I. A. 1965 *Handbook of Mathematical Functions: With Formulas, Graphs, and Mathematical Tables*. Dover.

Arfken, G. B. 1970 *Mathematical Methods for Physicists*. Academic.

Bertozzi, A. L. & Pugh, M. C. 1998 Long-wave instabilities and saturation in thin film equations. *Commun Pure Appl. Maths* **51**, 625–661.

Bico, J. & Queré, D. 2002 Rise of liquids and bubbles in angular capillary tubes. *J. Colloid. Interface Sci.* **247**, 162–166.

Eggers, J. & Dupont, T. F. 1994 Drop formation in a one-dimensional approximation of the Navier-Stokes equation. *J. Fluid Mech.* **262**, 205–221.

Grotberg, J. B. 1994 Pulmonary flow and transport phenomena. *Annu. Rev. Fluid Mech.* **26**, 529–571.

Hazel, A. L. & Heil, M. 2002 The steady propagation of a semi-infinite bubble into a tube elliptical or rectangular cross-section. *J. Fluid Mech.* **470**, 91–114.

Heil, M. & White, J. P. 2002 Airway closure: surface-tension-driven non-axisymmetric instabilities of liquid-lined elasitc rings. *J. Fluid Mech.* **462**, 79–109.

Hosoi, A. E. & Mahadevan, L. 1999 Axial instability of a free surface front in a partially-filled rotating cylinder. *Phys. Fluids* **11**, 97–106.

Huppert, H. E. 1982 The propagation of two-dimensional and axisymmetric viscous gravity currents over a rigid horizontal surface. *J. Fluid Mech.* **121**, 43–58.

Jensen, O. E., Chini, G. P. & King, J. R. 2004 Thin film flows near isolated humps and interior corners. *J. Engng Maths* **50**, 289–309.

Kalliadasis, S., Bielarz, C. & Homsy, G. M. 2000 Steady free-surface thin film flows over topography. *Phys. Fluids* **12**, 1889–1898.

Kistler, S. F. & Scriven, L. E. 1983 Coating flows. In *Computational Analysis of Polymer Processing* (ed. J. Pearson & S. Richardson). London: Applied Science Publishers.

Kolb, W. B. & Cerro, R. L. 1993*a* Film flow in the space between a circular bubble and a square tube. *J. Colloid. Interface Sci.* **159**, 302–311.

Kolb, W. B. & Cerro, R. L. 1993*b* The motion of long bubbles in tubes of square cross section. *Phys. Fluids* A **5**, 1549–1557.

Landau, L. D. & Levich, B. 1942 Dragging of a liquid by a moving plate. *Acta Physicochimica URSS* **17**, 42–54.

Landau, L. D. & Lifschitz, E. M. 1987 *Fluid Mechanics*. Pergamon.

Mazouchi, A. & Homsy, G. M. 2001 Free surface stokes flow over topography. *Phys. Fluids* **13**, 2751–2761.

Moffatt, H. K. 1964 Viscous and resistive eddies near a sharp corner. *J. Fluid Mech.* **18**, 1–18.

Moriarty, J. A. & Terrill, E. L. 1996 Mathematical modelling of the motion of hard contact lenses. *Eur. J. Appl. Maths* **7**, 575–594.

Myers, T. G. 1998 Thin films with high surface tension. *SIAM Rev.* **40**, 441–462.

Myers, T. G. 2003 Unsteady laminar flow over a rough surface. *J. Engng Maths* **46**, 111–126.

Olagunju, D. O. 1999 A 1-D theory for extensional deformation of a viscoelastic filament under exponential stretching. *J. Non-Newtonian Fluid Mech.* **87**, 27–46.

Oron, A., Davis, S. H. & Bankoff, S. G. 1997 Long-scale evolution of thin liquid films. *Rev. Mod. Phys.* **69**, 931–980.

Press, W. H., Teukolsky, S. A., Vetterling, W. T. & Flannery, B. P. 1992 *Numerical Recipes in Fortran: The Art of Scientific Computing*. Cambridge University Press.

Rosenzweig, J. & Jensen, O. E. 2002 Capillary-elastic instabilities of liquid-lined lung airways. *J. Biomech. Engng* **124**, 650–655.

Roy, R. V., Roberts, A. J. & Simpson, M. E. 2002 A lubrication model of coating flows over a curved substrate in space. *J. Fluid Mech.* **454**, 235–261.

Ruschak, K. J. 1978 Flow of a falling film into a pool. *AIChE J.* **24**, 705–708.

Schultz, W. W. 1987 Slender viscoelastic fiber flow. *J. Rheol.* **31**, 733–750.

Schwartz, L. W. & Weidner, D. E. 1995 Modeling of coating flows on curved surfaces. *J. Engng Maths* **29**, 91–103.

Spiegelberg, S. H. & McKinley, G. H. 1996 Stress relaxation and elastic decohesion of viscoelastic polymer solutions in extensional flow. *J. Non-Newtonian Fluid Mech.* **67**, 49–76.

Stillwagon, L. E. & Larson, R. G. 1988 Fundamentals of topographic substrate leveling. *J. Appl. Phys.* **63**, 5251–5258.

Stillwagon, L. E. & Larson, R. G. 1990 Leveling of thin films over uneven substrates during spin coating. *Phys. Fluids* A **2**, 1937–1944.

Stocker, R. & Hosoi, A. E. 2004 Corner flow in free liquid films. *J. Engng Maths* **50**, 267–288.

Thulasidas, T. C., Abraham, M. A. & Cerro, R. L. 1995 Bubble-train flow in capillaries of circular and square cross section. *Chem. Engng Sci.* **50**, 183–199.

Wasan, D. T., Koczo, K. & Nikolov, A. D. 1994 Mechanisms of aqueous foam stability and antifoaming action with and without oil: a thin film approach. In *Foams: Fundamentals and Applications in Petroleum Industry* (ed. L. L. Schramm), pp. 47–114. American Chemical Society, Washington.

Weislogel, M. M. 2001 Capillary flow in interior corners: The infinite column. *Phys. Fluids* **13**, 3101–3107.

Weislogel, M. M. & Lichter, S. 1998 Capillary flow in an interior corner. *J. Fluid Mech.* **373**, 349–378.

Wong, H., Fatt, I. & Radke, C. J. 1996 Deposition and thinning of the human tear film. *J. Colloid. Interface Sci.* **184**, 44–51.

Wong, H., Radke, C. J. & Morris, S. 1995 The motion of long bubbles in polygonal capillaries. Part 1. Thin films. *J. Fluid Mech.* **292**, 71–94.

Yiantsios, S. G. & Higgins, B. G. 1989 Rayleigh-taylor instability in this viscous films. *Phys. Fluids* A **1**, 1484–1501.